Down-conversion of electronic frequencies and their dephasing dynamics: Interferometric four-wave-mixing spectroscopy with broadband light

Jason C. Kirkwood and A. C. Albrecht
Department of Chemistry, Baker Laboratory, Cornell University, Ithaca, New York 14853
(Received 11 August 1999; published 10 February 2000)

The theory for temporally multidimensional, electronically resonant four-wave-mixing (FWM) spectroscopy based on broadband light interferometry is developed. Both homodyne and heterodyne detection are considered. Upon spectrally resolving the signal, the electronic Bohr frequency is seen to be extremely down-converted, even to zero frequency, but only with homodyne detection. These very low frequency fringes, referred to as radiation difference oscillations, are well known in the interferometric coherent Raman broadband light spectroscopies. Such low frequency fringes permit interferometry in the optical region using Nyquist criteria corresponding to far infrared sampling rates. Possible applications are illustrated by simulations of the two-dimensional third order signals from an electronic two-level system in a variety of ''baths.'' It is seen how homogeneous and inhomogeneous line-shaping mechanisms manifest themselves differently and revealingly in the free induction decay, the photon echo decay and their cross term components of the FWM signal.

PACS number(s): 42.65.Hw, 42.50.Md, 42.62.Fi

I. INTRODUCTION

A long established four-wave-mixing (FWM) phenomenon, the photon echo [1–7], has proven to be a powerful technique for exploring dynamics in the condensed phase. FWM echo experiments based on modern femtosecond lasers may involve as many as three different time parameters (the time intervals between the four waves) and probe ''bath'' dynamics that affect vibronic coherences in the visible (optical) region, or vibrational coherences in the infrared, as these are created across an ensemble of ''chromophores.'' Vibrational coherences are also studied in the optical region through the Raman effect [8–15]. In order for these vibrational coherences to provide insight into dynamics at the same level as that available in the FWM echo, one must turn to higher order Raman wave-mixing experiments [16,17]. However, it has been found that unlike FWM, their interpretation is easily complicated by competing cascaded events of lower order [18–24].

Concurrently with such widely applied femtosecond exploration of material dynamics, a very different approach has appeared in a few laboratories [25–31], including our own [32–44]. It is based on the interferometric manipulation of nontransform limited broadband (''noisy'') light having autocorrelation times on the femtosecond scale. Such a ''noisy'' light source is usually derived from a dye laser modified to permit oscillation over almost the entire bandwidth of the broadband source. In fact, its spectrum is very close to that of a transform limited femtosecond laser pulse, the fundamental difference being that the latter is *phase coherent* over its spectrum while the noisy light is *phase random* over its spectrum. Invariably the noisy light source is split into twin beams which are usually joined by a monochromatic source to polarize the sample. Ultrafast time resolution is achieved as the time separation of the twin noisy beams is interferometrically tuned on the femtosecond to picosecond time scale. The polarization of the ensemble carries the imprint of the noisy field which it retains for the coherence time of the polarized sample. The stored polarization is probed by the delayed twin beam which recognizes its own noise pattern imprinted in the material coherence with good interferometric contrast as long as the coherence can survive in the presence of phase disrupting dynamics of the system.

It turns out that for every conventional nonlinear spectroscopy—purely frequency domain or purely time domain—one can design its complete time-frequency interferometric spectroscopic counterpart. While the first application of noisy light to ultrafast timing was in the FWM vibronic echo experiment (with only one time parameter) [25], almost all subsequent work has been directed to the study of vibrational coherences driven optically by Raman resonances (the coherent Raman spectroscopies) [32–46]. Vibrational frequencies corresponding to more than 3000 cm^{-1} have been down-converted to zero to tens of cm^{-1} in the form of RDOs [41]. Upconversion of low-frequency vibrations through RDOs has also been demonstrated by appropriate tailoring of the noisy light spectrum [47–49].

The aim of the present manuscript is to revisit the FWM echo and (third order) free-induction decay (FID) experiments based on noisy light [25,50] with new theoretical insight. We consider the use of three distinct beams, or triplets, of the same noisy light source to polarize the sample. Two (interferometric) time parameters appear as the time separators between these fields. Also, unlike in the original experiment, here spectral resolution of the signal is taken to be essential. Both homodyne and heterodyne detection are considered. It is seen how only in the former case do RDOs appear. These represent electronic Bohr frequencies that are extremely down-converted into the zero to tens of cm^{-1} range—the first such phenomenon to our knowledge. For analytic simplicity, the usual two-level (electronic) model is examined rather than introducing a more complicated (but more realistic) two-vibronic manifold model as the basis for the material response function [51–53]. To illustrate applications of these new proposed experiments to dynamics—or the line shaping function—the standard model that includes both inhomogeneous (static) and homogenous (dynamic) line

broadening effects is built into the theory. This noisy light based interferometric spectroscopy is temporally two-dimensional (2D) (interferometric time delays τ and σ) and leads to 2D interferograms that are distinct for each detected frequency. Examples of these are given and it is shown how electronic line-shaping dynamics can be revealed from the extremely down-converted electronic frequencies by this new type of experiment.

First the full theory is developed for homodyne detection. It begins with the usual development of the third-order polarization just as for any cw FWM experiment. Then there appears an added layer of theory because of the noise content of the incident light. One must properly average over the stochastic noise contained in the noisy field amplitudes, which must be carried out at the intensity level of the signal. Previously developed factorized time correlators (FTCs) are used diagrammatically to help in this averaging. Their use also enables one to organize and estimate the relative strengths of the many terms that arise in such averaging. Following the introduction of the FTC diagrams, the next section is highlighted by simulated 2D representations of the (strongly down-converted) homodyne detected signal from which distinguishing characteristics of the two line broadening mechanisms become evident. Finally, application is made to heterodyne detection, where interpretation of the (now rapidly oscillating) signal is discussed.

II. THEORETICAL CONSIDERATIONS

As with any spectroscopy, the fundamental quantity in determining the FWM signal is the appropriate nonlinear optical polarization. At the start, the usual approach for cw FWM is outlined. In the present treatment, three broadband nontransform limited noisy light beams B, B', and B'', each along separate wave vectors $\mathbf{k}_B$, $\mathbf{k}_{B'}$, and $\mathbf{k}_{B''}$ are employed. Their corresponding (real) fields are given by $\frac{1}{2}(E_j+E_j^*)$, $j=B$, B', B'', respectively. This configuration allows one to control the relative delay between B and $B'(\tau)$ and between B and $B''(\sigma)$. We choose the fourth wave, the signal ($\mathbf{k}_s$), as the one which carries the distinct wave vector given by $\mathbf{k}_s=\mathbf{k}_B+\mathbf{k}_{B'}-\mathbf{k}_{B''}$. Such a signal is produced by the *in-phase* action of B and B' and these together acting *conjugately* with respect to B''.

The complex scalar fields associated with B, B' and B'' at time t are

$$E_B(t)=p(t)e^{-i\varpi t}, \tag{1}$$

$$E_{B'}(t)=p(t-\tau)e^{-i\varpi(t-\tau)}, \tag{2}$$

$$E_{B''}(t)=p(t-\sigma)e^{-i\varpi(t-\sigma)}. \tag{3}$$

The noise function $p(t)$ is taken to be a complex ergodic stochastic function of t, which is assumed to obey complex circular Gaussian statistics [54,55].

To describe the macroscopic polarization at third order, we employ wave-mixing energy level (WMEL) diagrams [8,56,57]. Formally equivalent to dual sided Feynman diagrams, their representation is particularly helpful in clearly exposing light-matter resonances. In these diagrams, dashed vertical arrows (up or down) represent bra-side evolution, while solid vertical arrows (up or down) denote the ket-side evolution of the density matrix. The material eigenstates subject to resonances are represented by solid horizontal lines.

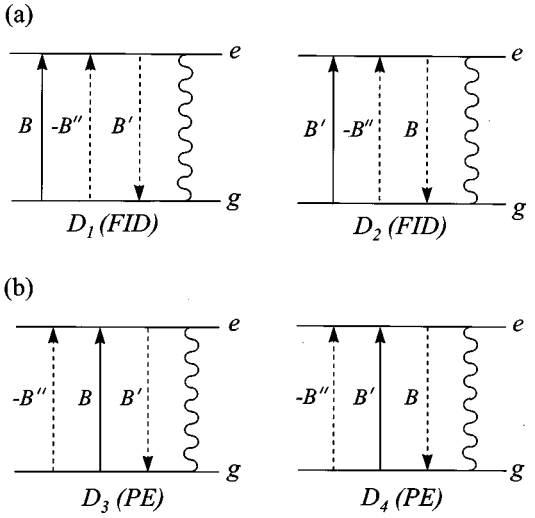

FIG. 1. The WMEL diagrams describing the four fully resonant third order Liouville pathways. Solid arrows represent ket-side evolution of the density matrix, while dashed arrows denote bra-side evolution. The wavy line is the emitted signal field. (a) The two free induction decay (FID) Liouville pathways and (b) the two photon echo (PE) Liouville pathways.

In general, the number of WMEL (or Feynman) diagrams at nth order (for cw experiments) corresponds to the number of Liouville pathways 2^n multiplied by the number of distinct temporal field orderings (as many as $n!$) for the given process. Therefore, at third order, where B, B', and B'' are distinct, there are $2^3 3!=48$ different WMEL diagrams at the polarization level. However, we limit the present treatment only to the four maximally (triply) resonant diagrams which generate a signal along $\mathbf{k}_S=\mathbf{k}_B+\mathbf{k}_{B'}-\mathbf{k}_{B''}$ (see Fig. 1). Other diagrams correspond to Liouville pathways less resonant, or entirely nonresonant, which should at least be minor contributions to the resonant signal. (In fact, four other diagrams satisfy the resonance and phase matching conditions, yet do not conserve the trace of the density matrix [50]. If one imposes the conservation of the trace on these four diagrams, it is seen that they are entirely equivalent to the four presented here, and are treated accordingly in the present calculations.)

Thus the fully resonant, third-order polarization is given by

$$\overline{P}^{(3)}(t,\tau,\sigma,\omega_{eg}^t)\propto N[D_1+D_2+D_3+D_4], \tag{4}$$

where N is the number density of the resonant molecules and the D_i's are the light-matter interaction functions represented by the four WMEL diagrams illustrated in Fig. 1. Diagram D_1 [Fig. 1(a)] is represented analytically by

$$D_1 \propto \int_{-\infty}^{t} dt_3 \int_{-\infty}^{t_3} dt_2 \int_{-\infty}^{t_2} dt_1 \times R^{(3)}_{\mathrm{FID}}(t_1,t_2,t_3,\omega^t_{eg}) E_B(t_1) E^*_{B''}(t_2) E_{B'}(t_3), \quad (5)$$

where $R^{(3)}_{\mathrm{FID}}(t_1,t_2,t_3,\omega^t_{eg})$ is the time-dependent portion of the third order material response function

$$R^{(3)}_{\mathrm{FID}}(t_1,t_2,t_3,\omega^t_{eq}) = e^{(-i\omega^t_{eg}-\gamma_{eg})(t_2-t_1)} e^{-\gamma_{ee}(t_3-t_2)} e^{(-i\omega^t_{eg}-\gamma_{eg})(t-t_3)}. \quad (6)$$

Here γ_{eg} represents the dephasing rate constant for the coherence loss between states $|e\rangle$ and $|g\rangle$, while γ_{ee} is the population relaxation rate constant for excited state $|e\rangle$. The Bohr frequency for this two-level system is given by ω^t_{eg} (in which the *t* superscript identifies the Bohr frequency as the one involved in ''*t*-timeline'' evolution). (See below for ''*s*-timeline'' evolution.) The expression for D_2 is identical to that of D_1, only the actions of E_B and $E_{B'}$ are temporally permuted.

Equation (6) is valid when the nuclear dynamics associated with the bath have correlation times shorter than the reciprocal of their root mean square (rms) modulation of the Bohr frequency—the so-called fast modulation limit. The effects of this class of nuclear motions are referred to as being homogeneous in nature, since they reflect the ensemble-averaged dynamics of the bath.

In diagram D_1 (D_2), the initial field action, B (B') creates a ket-state coherence between the ground electronic state $|g\rangle$ and the excited electronic state $|e\rangle$. This ket-side field action promotes the density matrix from its initial equilibrium state $\rho^{(0)}_{gg}$ to $\rho^{(1)}_{eg}$. This coherence is allowed to evolve freely (with a dephasing rate constant of γ_{eg}) until the second field action $-B''$ intervenes (now on the bra side) at a later time. In our simple two-level model, the second field action creates an excited state population by promoting the density matrix from $\rho^{(1)}_{eg}$ to $\rho^{(2)}_{ee}$. This population is allowed to relax (with rate constant γ_{ee}) until the final field action $B'(B)$ takes the density matrix from $\rho^{(2)}_{ee}$ to $\rho^{(3)}_{eg}$. One may notice that this coherence is identical (in phase) to the coherence created at first order $\rho^{(1)}_{eg}$. The signal field (denoted by the wavy line) is then subsequently launched at $\omega_S = \omega^t_{eg}$. As will be seen, the terms associated with diagrams D_1 and D_2 are unable to rephase the inhomogeneous contributions to the third order signal and as such are referred to as the (third-order) free-induction-decay (FID) terms.

In contrast to the FID diagrams, the remaining two do posses rephasing capabilities and will be referred to as the photon-echo (PE) diagrams. These are given by diagrams D_3 and D_4, which are represented analytically as

$$D_3 \propto \int_{-\infty}^{t} dt_3 \int_{-\infty}^{t_3} dt_2 \int_{-\infty}^{t_2} dt_1 \times R^{(3)}_{\mathrm{PE}}(t_1,t_2,t_3,\omega^t_{eg}) E^*_{B''}(t_1) E_B(t_2) E_{B'}(t_3), \quad (7)$$

where the time-dependent part of the material response function is

$$R^{(3)}_{\mathrm{PE}}(t_1,t_2,t_3,\omega^t_{eg}) = e^{(i\omega^t_{eg}-\gamma_{eg})(t_2-t_1)} e^{-\gamma_{ee}(t_3-t_2)} e^{(-i\omega^t_{eg}-\gamma_{eg})(t-t_2)}. \quad (8)$$

The expression for D_4 is given by Eq. (7), only with the actions of E_B and $E_{B'}$ temporally permuted. As seen in Fig. 1(b), the first field action ($-B''$) now creates a bra-side coherence by taking the density matrix from its initial equilibrium state $\rho^{(0)}_{gg}$ to $\rho^{(1)}_{ge}$. The density matrix elements at second and third order ($\rho^{(2)}_{ee}$ and $\rho^{(3)}_{eg}$), through subsequent actions of B' and B, are equivalent to those found in the FID diagrams. It is seen that the phase of the coherence at first order $\rho^{(1)}_{ge}$ is now conjugate to that at third order $\rho^{(3)}_{eg}$ thus allowing for rephasing of the inhomogeneous contributions to the signal.

The usual model for such heterogeneous contributions is applied. The assembly of chromophores is taken to have different transition frequencies because of a static (on the timescale of the experiment) distribution of local environments. This static inhomogeneous distribution of the Bohr frequency of the two-level system reflects the heterogeneity of the system and carries no immediate dynamical information. The third-order optical polarization must now be written as one averaged over the static heterogeneity

$$P^{(3)}(t,\tau,\sigma) = \int_0^\infty d\omega^t_{eg} g(\omega^t_{eg}) \overline{P}^{(3)}(t,\tau,\sigma,\omega^t_{eg}), \quad (9a)$$

where the Bohr frequency, ω^t_{eg} is distributed using the normalized function $g(\omega^t_{eg})$ centered about frequency ω^0_{eg}.

Most often, the optical spectroscopies are detected in quadrature (homodyne detection). That is, the signal at the detector is derived from the squared modulus of the sum of all fields generated from the huge number of polarized chromophores. Thus, the quadrature detected signal is effectively built from the product of all polarization fields derived from all pairs of chromophores [32,39]. This ''bichromophoric model'' is particularly important to the noisy light spectroscopies where stochastic averaging must be carried out at the signal level [58]. As will be seen, the only correlations that survive the intensity level averaging are between noisy light induced polarization events on one chromophore (evolving under timeline *t*) and their conjugate events on a second chromophore (evolving under a distinct timeline *s*), whose inhomogeneously distributed third order polarization is written [as in Eq. (9a)]

$$P^{(3)}(s,\tau,\sigma) = \int_0^\infty d\omega^s_{eg} g(\omega^s_{eg}) \overline{P}^{(3)}(s,\tau,\sigma,\omega^s_{eg}). \quad (9b)$$

The signal intensity is given by

$$I^{(3)}(\tau,\sigma)\propto\frac{1}{T}\int_{-T/2}^{T/2}dt\int_{-\infty}^{\infty}d\omega_s\mathcal{D}_S(\omega_s)\int_{-\infty}^{\infty}dse^{i\omega_S(t-s)}\times P^{(3)}(t,\tau,\sigma)P^{*(3)}(s,\tau,\sigma),\tag{10}$$

where $\mathcal{D}_S(\omega_S)$ and T are the intensity level spectral response function and signal averaging time of the detector, respectively. In the limit that T is much longer than any dynamical variable ($T\rightarrow\infty$) and the signal (ω_S) is monochromatically detected at ω_D, [$\mathcal{D}_S(\omega_S)=\delta(\omega_S-\omega_D)$], Eq. (10) reduces to

$$I^{(3)}(\omega_D,\tau,\sigma)\propto\int_{-\infty}^{\infty}d(t-s)e^{i\omega_D(t-s)}\times\langle P^{(3)}(t,\tau,\sigma)P^{*(3)}(s,\tau,\sigma)\rangle,\tag{11}$$

where $\langle\cdots\rangle$ denotes a stochastic average over the noisy fields at the signal level. Substituting Eqs. (4) and (9a) into Eq. (11) gives

$$I^{(3)}(\omega_D,\tau,\sigma)\propto N^2\int_{-\infty}^{\infty}d(t-s)e^{i\omega_D(t-s)}\tag{12a}$$

$$\times\int_0^{\infty}d\omega_{eg}^t g(\omega_{eg}^t)\int_0^{\infty}d\omega_{eg}^s g^*(\omega_{eg}^s)$$

$$\times\{\langle D_1D_1^*\rangle+\langle D_2D_2^*\rangle+2\,\mathrm{Re}\langle D_1D_2^*\rangle\tag{12b}$$

$$+\langle D_3D_3^*\rangle+\langle D_4D_4^*\rangle+2\,\mathrm{Re}\langle D_3D_4^*\rangle\tag{12c}$$

$$+[2\,\mathrm{Re}\langle D_1D_3^*\rangle+2\,\mathrm{Re}\langle D_1D_4^*\rangle+2\,\mathrm{Re}\langle D_2D_3^*\rangle+2\,\mathrm{Re}\langle D_2D_4^*\rangle]\}.\tag{12d}$$

Although not exposed in the above expression (but to appear explicitly below), down-converted representations of the electronic transition, referred to as radiation difference oscillations (RDOs), manifest themselves in the homodyne detected signal. These RDOs are given the frequency label Δ and for the present case are equal to $\omega_D-\omega_{eg}^0$. Thus if one were to monochromatically detect the optical signal at frequency ω_{eg}^0, the RDO would be identically zero, and one achieves complete down-conversion (to zero frequency) of the electronic transition. This is of particular importance since the Nyquist criterion for successful interferometry is satisfied for very much smaller sampling rates than would be required for optical interferometry. Thus, even though the signal is optical (oscillating at a frequency ω_{eg}^0), the minimum step size for adequate interferometric sampling of these RDOs is much larger than that required for more conventional interferometric techniques. As will be seen, this is not the case in heterodyne detection of the signal where RDOs do not appear, but oscillations at optical frequencies are present.

A. Free induction decay (FID) at the quadrature level

Unlike the femtosecond FWM experiments, the two classes of Liouville pathways (or WMEL diagrams)—the FID and PE—may not be separated experimentally through any time delay manipulation. The three broadband fields are from the same nanosecond laser and are better regarded as ''continuous wave'' (Effectively, the temporal duration of the fields is much longer than any physical time scales under study). Although they cannot be experimentally separated, we examine their contributions to the total third order signal individually, only to remember that the polarization is a superposition of all Liouville paths simultaneously occurring, both FID and PE. With homodyne detection, cross terms between these must arise.

We first examine the quadrature FID terms given in Eq. (12b). Inserting the analytic expression for diagrams D_1 and D_2, one has

$$I_{\mathrm{FID}}^{(3)}(\omega_D,\tau,\sigma)\propto N^2\int_{-\infty}^{\infty}d(t-s)e^{i\omega_D(t-s)}\int_0^{\infty}d\omega_{eg}^t g(\omega_{eg}^t)\times\int_0^{\infty}d\omega_{eg}^s g^*(\omega_{eg}^s)\int d\Omega_t\int d\Omega_s\times\sum_{i=1}^{4}\Gamma_i^{(3,3)}e^{-i\varpi(t_3-s_3)}\times e^{i\varpi(t_2-s_2)}e^{-i\varpi(t_1-s_1)}\times R_{\mathrm{FID}}^{(3)}(t_1,t_2,t_3,\omega_{eg}^t)R_{\mathrm{FID}}^{*(3)}(s_1,s_2,s_3,\omega_{eg}^s),\tag{13}$$

where $\int d\Omega_j$ represents the integral over the three time variables associated with the field actions on timeline $j(t,s)$:

$$\int d\Omega_j=\int_{-\infty}^{j}dj_3\int_{-\infty}^{j_3}dj_2\int_{-\infty}^{j_2}dj_1.\tag{14}$$

Here $\Gamma_i^{(3,3)}$ is a six-point correlation function of the random noise functions associated with the noisy fields. The subscript i simply labels the individual correlation functions. [The four six-point correlations functions which describe the quadrature FID process are assigned the notation $\Gamma_i^{(3,3)}$ ($i=1,\ldots,4$).] The time dependence of these correlation function is suppressed for convenience, yet it should be understood that they depend on all six time variables (each in a different manner), as well as the two interferometric delay times, τ and σ. Their explicit form is given in the Appendix.

B. Photon echo at the quadrature level

The expression for term (12c) becomes

$$I^{(3)}_{\mathrm{PE}}(\omega_D,\tau,\sigma)\propto N^2\int_{-\infty}^{\infty}d(t-s)e^{i\omega_D(t-s)}\int_0^{\infty}d\omega^t_{eg}g(\omega^t_{eg})\times\int_0^{\infty}d\omega^s_{eg}g^*(\omega^s_{eg})\int d\Omega_t\int d\Omega_s\times\sum_{i=5}^{8}\Gamma^{(3,3)}_i e^{-i\varpi(t_3-s_3)}\times e^{-i\varpi(t_2-s_2)}e^{i\varpi(t_1-s_1)}\times R^{(3)}_{\mathrm{PE}}(t_1,t_2,t_3,\omega^t_{eg})R^{*(3)}_{\mathrm{PE}}(s_1,s_2,s_3,\omega^s_{eg}) \tag{15}$$

upon insertion of Eq. (7). The four six-point time correlation functions for the PE process are labeled $\Gamma^{(3,3)}_i$ $(i=5,\ldots,8)$ and are given in the Appendix.

C. The FID-PE cross terms

Unlike heterodyne detected signals, those at the quadrature (homodyned) level not only contain the quadrature FID and PE terms but also the cross terms between the FID and PE pathways. These FID-PE cross terms [term (12d)] become

$$I^{(3)}_{\mathrm{FID\text{-}PE}}(\tau,\sigma)\propto 2N^2\int_{-\infty}^{\infty}d(t-s)e^{i\omega_D(t-s)}\int_0^{\infty}d\omega^t_{eg}g(\omega^t_{eg})\times\int_0^{\infty}d\omega^s_{eg}g^*(\omega^s_{eg})\int d\Omega_t\int d\Omega_s\times\sum_{i=9}^{12}\Gamma^{(3,3)}_i e^{-i\varpi(t_3-s_3)}\times e^{i\varpi(t_2+s_2)}e^{-i\varpi(t_1+s_1)}\times\mathrm{Re}[R^{(3)}_{\mathrm{FID}}(t_1,t_2,t_3,\omega^t_{eg})\times R^{*(3)}_{\mathrm{PE}}(s_1,s_2,s_3,\omega^s_{eg})] \tag{16}$$

upon inserting the expressions for the polarization, Eqs. (5) and (7). Here eight six-point time correlation functions are needed to entirely describe the FID-PE cross terms. These are labeled $\Gamma^{(3,3)}_i$ $(i=9,...,16)$. However, the latter half of these $[\Gamma^{(3,3)}_i$ $(i=13,...,16)]$ represents noise correlations that are complex conjugates to those described by the first half $[\Gamma^{(3,3)}_i$ $(i=9,...,12)]$. For this reason, it is sufficient to concern ourselves with $\Gamma^{(3,3)}_i$ $(i=9,...,12)$ and in the end take the real part of their contribution [called for in Eq. (16)].

To proceed, it is necessary to properly handle these six-point time correlation functions found in Eqs. (13), (15), and (16). As previously stated, the random functions $p(t)$ of the complex noisy fields are taken to obey complex Gaussian statistics. This assumed nature of the noise allows one to employ the complex Gaussian moment theorem (CGMT), which states that all higher order correlators can be expressed in terms of products of pair correlators [54,55]. Thus any given $2n$-point correlator $\Gamma^{(n,n)}_i$ may be decomposed into the sum of $n!$ terms, each consisting of the product of n two-point correlators $\Gamma^{(1,1)}$. As noted, sets of these products of two-point time correlators may be conveniently handled by factorized time correlator diagram analysis.

III. FTC DIAGRAM ANALYSIS

A FTC diagram is a symbolic representation of any given product of two-point time correlators. The general rules for the construction of FTC diagrams for any noisy light spectroscopy have been given elsewhere [59–61], however a brief synopsis is presented.

Each FTC diagram consists of a set of two vertically displaced, parallel, horizontal lines, *t* for one chromophore, *s* for another, denoting the evolution timelines for the two independent macroscopic polarizations developed on a generic ''bichromophoric pair.'' Imposed on these lines are tick marks (three on each for the current FWM process), each marking the moment of action of one of the fields on the chromophore. Any pair correlator is indicated by a segment. A given segment joins the two tick mark pairs involving conjugate actions of noisy fields. The autocorrelators (or ''self-correlators'') are designated by a single *line* joining a pair of tick marks. (These are B/B, B'/B' or B''/B'' autocorrelators which cannot depend on τ or σ.) Of the remaining three types of correlator segments, two are ''single headed''—headed either by an *arrow* or by a *solid* circle. The single headed segments refer to the B'/B and B''/B cross correlators. The former are τ dependent and each has an *arrow* as its single head. The latter are σ dependent, each having a *solid circle* as its head. The remaining pair correlator is the B''/B' cross correlators. Such correlators depend on $(\tau-\sigma)$ and their segment is double headed, the *arrow* points to the B' field and the *solid circle* is at the B'' tick mark end. Every triplet of pair-correlators (or FTC diagram) is represented by three segments built onto the two tick-marked time lines.

Complete WMEL and FTC diagram analyses for the homodyne detected FWM signal appear in the second column of Table I. From this table, it can be easily seen that after taking the four (triply resonant) WMEL diagrams to the quadrature level, one has sixteen possible pairwise contributions to the signal. The jth contribution is assigned its appropriate six-point time correlator $\Gamma^{(3,3)}_j$. The latter is decomposed into 3! products of pair correlators which form the basis of an FTC diagram. Thus altogether, one has to consider 96 FTC diagrams. (Similar analyses for the heterodyne detected signal is found in the third column of this table.)

For the present FWM process, 16 of the 96 FTC diagrams consist of just three line segments (the τ, σ-independent autocorrelators) in the homodyne detected signal. These need not be separately considered because their contribution may be obtained simply by setting $\tau,\sigma=0$ in the τ, σ-dependent diagrams. [At τ (or $\sigma=0$), all arrows (or solid circles) become lines.] These delay time-independent diagrams make up the constant background part of the signal. Such a constant background is characteristic of all quadrature detected noisy light spectroscopies. Thus for analytical convenience, this background is often subtracted from the homodyne

TABLE I. The WMEL and FTC diagram analyses for the electronically resonant FWM process.

	Intensity level (homodyne)	Intensity level (heterodyne)
	WMEL diagram analysis for both cw and noisy light FWM	
All Liouville pathways for CW $\chi^{(3)}$ experiments	48 WMELs$\times$48 WMELs $=2304$	48 WMELs$\times E_{lo}$ $=48$
Of which, the fully (triply) resonant Liouville pathways are	4 WMELs$\times$4 WMELs $=16$	4 WMELs$\times E_{lo}$ $=4$
	FTC diagram analysis (noisy light) for only the triply resonant pathways	
Time correlators	16 Six-point time correlators $\Gamma_1^{(3,3)},\ldots,\Gamma_{16}^{(3,3)}$	4 Four-point time correlators $\Gamma_1^{(2,2)},\ldots,\Gamma_4^{(2,2)}$
Decomposition into pair correlators	Each six-point correlator may be represented as the sum of 6 FTC diagrams[a]	Each four-point correlator may be represented as the sum of 2 FTC diagrams[b]
Total number of FTC diagrams	$16\times6=96$	$4\times2=8$

[a]For homodyne detection, each FTC diagram represents the product of three pair correlators $\Gamma_i^{(1,1)}\Gamma_j^{(1,1)}\Gamma_k^{(1,1)}$.
[b]For heterodyne detection, each FTC diagram represents the product of two pair correlators $\Gamma_i^{(1,1)}\Gamma_j^{(1,1)}$.

detected signal. (Though in considering the effective dynamic range of any noisy light experiment, it plays an important role.) In heterodyne detection, the constant background is absent (see below).

A. Free induction decay at the quadrature level

Enumeration of both the (triply resonant) WMEL and FTC diagrams for the individual processes are displayed in Table II for both homodyne and heterodyne detection. Such enumeration allows one to easily classify the entire set of FTC diagrams into their individual subsets, FID, PE, and FID-PE.

By application of the CGMT, the four six-point correlators associated with the FID process $\Gamma_i^{(3,3)}$ $(i=1,...,4)$, may be expressed as the sum of twenty-four $(3!\times4)$FTC diagrams, each representing a product of three two-point correlators (as seen in Table II).

For illustrative purposes, four of these FTC diagrams are shown in Fig. 2(a). Each diagram corresponds to one of six that follows from the decomposition of a single six-point correlator $\Gamma_i^{(3,3)}$ $(i=1,...,4)$. By making use of some conceptual tools associated with these diagrams [59–61], one may easily determine which noise correlations contribute most strongly to the signal, thus bypassing calculation of the less dominant (or even negligible) terms in the full theory. [The four diagrams in Fig. 2(a) are in fact the strongest of the twenty-four diagrams for the FID pathways.] It is also possible to determine which of the noise correlations contribute

TABLE II. The enumeration of WMEL and FTC diagrams representing the FID, PE, and cross terms for the triply resonant Liouville pathways.

	Intensity level (homodyne)			Intensity level (heterodyne)		
	The WMEL diagram enumeration					
Fully (triply) resonant Liouville pathways	FID	PE	cross	FID	PE	cross
	4	4	8	2	2	
	The FTC diagram enumeration					
Time correlators	FID	PE	cross	FID	PE	cross
	$\Gamma_1^{(3,3)},\ldots,\Gamma_4^{(3,3)}$	$\Gamma_5^{(3,3)},\ldots,\Gamma_8^{(3,3)}$	$\Gamma_9^{(3,3)},\ldots,\Gamma_{16}^{(3,3)}$	$\Gamma_1^{(2,2)},\Gamma_2^{(2,2)}$	$\Gamma_3^{(2,2)},\Gamma_4^{(2,2)}$	
	Six-point correlators			Four-point correlators		
Total number of FTC diagrams	FID	PE	cross	FID	PE	cross
	24	24	48	4	4	
	96 total FTC diagrams, each being the product of 3 pair correlators, $\Gamma_i^{(1,1)}\Gamma_j^{(1,1)}\Gamma_k^{(1,1)}$			8 total FTC diagrams, each being the product of 2 pair correlators, $\Gamma_i^{(1,1)}\Gamma_j^{(1,1)}$		

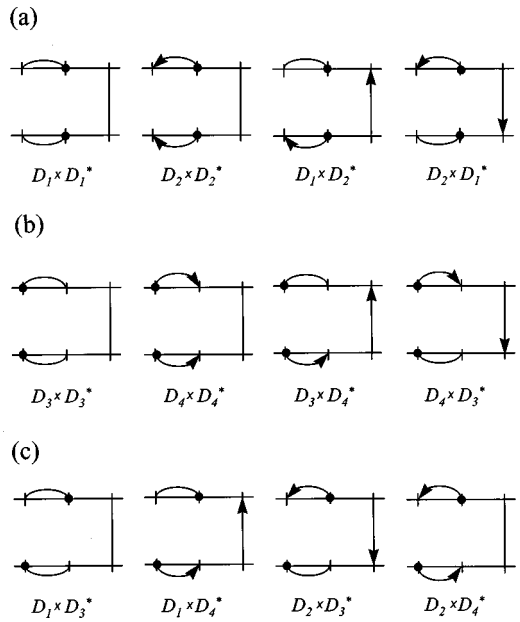

FIG. 2. Twelve (of 96) FTC diagrams for the homodyne detected FWM process. The top horizontal line represents the *t* timeline while the lower line is the *s* timeline. Each tick marks the time when a field intervenes ($t_1<t_2<t_3$; $s_1<s_2<s_3$; time increases from left to right in the polarization process). The arrows (solid circles) ''point'' to the time at which the τ (σ) shifted field, $B'(B'')$, acts, while the tail denotes the time at which field *B* acts. The FTC diagrams describing noise correlations for the (a) quadrature FID, (b) quadrature PE, and (c) FID-PE *cross* term processes. Each diagram is identified by the product of the two WMEL diagrams whose light-matter interactions are being represented.

to the signal at any given set of values of the delay times. If the arrowhead ''points'' to the left, then the FTC diagram is nonzero for $\tau<0$. If the solid circle head is to the left, then the FTC diagram is nonzero for $\sigma<0$. Conversely, if the ''heads'' are on the right, then the FTC diagram is nonzero for $\tau>0$ (arrows) or $\sigma>0$ (solid circle). This analysis must be done for both the *t* and *s* timelines.

Thus, the first diagram in Fig. 2(a) (FID, $D_1\times D_1^*$) is nonzero only when $\sigma>0$, since the solid circles on both the *t* and *s* timelines ''point'' to the right. Physically, this diagram represents noise correlations which allow accumulation (integration) over both the *t* and *s* timelines only for $\sigma>0$. Likewise, the second diagram (FID, $D_2\times D_2^*$) is nonzero for $(\sigma-\tau)>0$, as inferred from the direction of the arrow (solid circle) heads. The final two FTC diagrams contribute when both inequalities $\sigma>0$ and $(\sigma-\tau)>0$ are simultaneously satisfied, since noise correlations on the *t* timeline only allow accumulation for one time domain, while the noise correlations on the *s* timelines permit accumulation for the other. Since these FTC diagrams represent products of pair correlators, both time domains must be satisfied simultaneously.

Twelve of the remaining sixteen delay time-dependent FTC diagrams for the quadrature FID pathways contribute either to one of the three time domains mentioned above or to one of the following domains: $\sigma<0$, $(\tau-\sigma)>0$, $\sigma<0$ and $(\tau-\sigma)>0$, $(\tau-\sigma)>0$, and $\sigma>0$, or $(\sigma-\tau)>0$ and $\sigma<0$. Simply stated, the entire set of quadrature FID FTC diagrams represent noise correlations which allow for full accumulation over the two independent timelines for the entire $\tau-\sigma$ space. (At present, we have excluded discussion about the remaining four delay time-dependent FTC diagrams, each of which contributes to either the $\tau>0$ or $\tau<0$ time domain, since they are predicted to be the weakest of all diagrams. However, one finds that their contribution becomes increasingly large in the limit where $\gamma_{eg}<\gamma_{ee}$. This will be appropriately addressed in Sec. IV.)

B. Photon echo at the quadrature level

Displayed in Fig. 2(b) are (the strongest) four of 24 FTC diagrams for the quadrature PE Liouville pathways (see Table II). Topologically similar to the quadrature FID FTC diagrams, these four diagrams represent contributions to the homodyned signal for the following delay time domains $\sigma<0$, $(\tau-\sigma)>0$, and $\sigma<0$ and $(\tau-\sigma)>0$. As it turns out, 12 of the remaining 16 delay time-dependent FTC diagrams (the four weakest, τ-dependent diagrams excluded) also contribute to one of the aforementioned time domains. Thus, the FTC diagrams for the quadrature PE pathways do not symbolize noise correlations which are free to accumulate over the two timelines, but those that are restricted to the $\sigma<0$ and $(\tau-\sigma)>0$ domains. One then finds that in the region where the two inequalities, $\sigma>0$ and $(\tau-\sigma)<0$, are both satisfied, the signal contains contributions only from the quadrature FID pathways. Thus a partial separability of PE and FID may, after all, be possible.

C. FID-PE cross terms

Four (of the 48) FTC diagrams for the FID-PE cross terms are shown in Fig. 2(c). These four FTC diagrams represent the noise correlation events on timeline *t* in Fig. 2(a) ''crossed'' with the noise correlation events on timeline *s* in Fig. 2(b). (Recall that one must add the complex conjugate of these FID-PE cross term diagrams to obtain a pure real expression.)

The first and last diagrams are identically zero since noise correlations on the *t* timeline (FID-like) are allowed to accumulate when $\sigma>0$ $[(\sigma-\tau)>0]$, while on the *s* timeline (PE-like), the noise correlations can only accumulate when $\sigma<0$ $[(\tau-\sigma)>0]$. The product of such noise correlations vanishes, and thus these diagrams do not contribute to the total signal. The two other diagrams are nonzero when $\sigma>0$ and $(\tau-\sigma)>0$, and $\sigma<0$ and $(\sigma-\tau)>0$, respectively. Accounting for the remaining 12 time delay dependent FTC diagrams (τ-only diagrams excluded), one finds that, as with the PE pathways, only in the delay time domains where $\sigma<0$ and $(\tau-\sigma)>0$ is the signal nonzero. Such analysis will permit one to easily characterize the two-dimensional signals presented in Sec. IV.

Interestingly, the entire set of FTC diagrams for the present situation is completely isomorphic with those that describe a fifth order (pseudo) Raman echo process presented in [21,62], as well as those describing a fifth order (vibrational population) process presented by Lau *et al.* [45,46]. This isomorphism will be treated in more detail in Ref. [62], yet it should be noted that only the noise correlations are

isomorphic, *not* the light-matter interactions described by the WMEL diagrams.

IV. SIMULATIONS OF THE HOMODYNE-DETECTED SIGNAL

In order to continue, it is necessary to specify the analytic forms for both the pair correlations functions $\Gamma^{(1,1)}$ (obtained from decomposition of the six-point time correlators—see the Appendix) and the static Bohr frequency distribution function $g(\omega_{eg})$. For analytic simplicity, we have chosen all pair correlators to be δ functions $[\Gamma^{(1,1)}(t_i-t_j)=\delta(t_i-t_j)]$. This corresponds to the ideal limit in which the autocorrelation time of the noisy light is much smaller than any physical time scale under study. The distribution function is taken to be Gaussian,

$$g(\omega_{eg})=\frac{1}{\sqrt{\pi}\Omega}e^{-(\omega_{eg}-\omega_{eg}^0)^2/\Omega^2}, \tag{17}$$

where Ω is a measure of the HWHM of the frequency distribution.

To perform the integration given in Eqs. (13), (15), and (16), one must now analytically continue the integrals into the complex plane and use contour integration. The analytic expression for the signal is quite complicated and lengthy and is not presented. Instead, we choose to display 2D representations of the signal for selected sets of parameters. There are three parameters $u\equiv\gamma_{ee}/\gamma_{eg}$, Δ, the RDO frequency and Ω, a measure of the width of the Gaussian distribution. When $u=0$, population relaxation plays no role in coherence dephasing. When $u=0.5$, both population decay and pure dephasing are important to coherence loss. Both cases are examined. The RDO frequency Δ is determined by the detected frequency ω_D. When the frequency of detection matches ω_{eg}^0, $\Delta=0$; when $\omega_D\neq\omega_{eg}^0$, $\Delta\neq0$. We examine both cases. Finally, inhomogeneity is varied from none, at $\Omega=0$, to its complete dominance as $\Omega\rightarrow\infty$.

In all of the simulations, the center frequency of the noisy light ϖ is taken to be in resonance with the mean electronic frequency $\omega_{eg}^0=2.64\times10^{15}$ Hz (or equivalently $\tilde{\nu}_{eg}^0\equiv\omega_{eg}^0/2\pi c=14\,000\,\mathrm{cm}^{-1}$). The entire set of 96 FTC diagrams is included in these simulations, even though only a small subset of them is shown in Fig. 2.

The $u=0$, $\Delta=0$ *case.* Shown in Fig. 3 is the third order homodyne detected signal (at $\Delta\equiv\omega_D-\omega_{eg}^0=0$) generated for a sample where $u=0$ and for the homogeneous limit ($\Omega=0$). The constant background always affiliated with homodyne detection is removed from this and subsequent figures. (The peak-to-background ratio—the interferometric contrast—actually depends on the magnitude of u as well as the region of the τ-σ plane that is being explored. Thus, a unique value cannot be stated for this spectroscopy. However, it is important to be reminded that, unlike the situation in the femtosecond pulsed nonlinear spectroscopies, this contrast ratio is in fact finite.) The two-dimensional representation in Fig. 3 is free of all oscillations since the electronic transition frequency has been completely down-converted to 0 ps^{-1}. One may also notice that the signal is nonzero in all four quadrants of the reduced τ-σ plane. [Of course the (background removed) signal does in fact decay to zero at large values of the delay times.] The exponential decays along the three principal axes, $\tau=0$, $\sigma=0$, $\sigma=\tau$ are $e^{-2\gamma_{eg}|\sigma|}$, $e^{-\gamma_{eg}|\tau|}$, $e^{-\gamma_{eg}|\tau|}$, respectively. After all, γ_{eg} is the only surviving rate constant in this simulation.

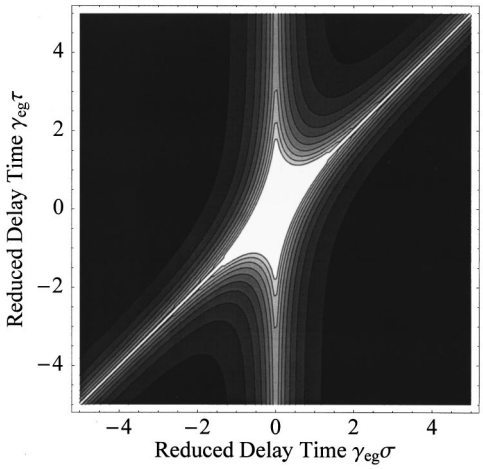

FIG. 3. A contour plot of the simulated homodyne third order signal in the homogeneous limit with $u=0$ and $\tilde{\Delta}=0\ \mathrm{cm}^{-1}$. Lighter regions indicate areas of higher intensity. The (background-subtracted) signal is nonzero for the entire τ-σ plane, and decays to zero for increasingly large values of delay times.

As one inhomogeneously distributes the electronic Bohr frequency (as a Gaussian) by making $\Omega>0$, the signal begins to exhibit a slight Gaussian decay along the three (partial) axes [$(\tau=0,\sigma<0)$, $(\sigma=0,\tau>0)$, and $(\sigma=\tau,\sigma,\tau<0)$], until the ratio Ω/γ_{eg} becomes sufficiently large ($\gg1$), when simple exponential decay again is recovered. In this limit of extreme heterogeneity, the exponential decays are given by $e^{(-4\gamma_{eg}/f_\sigma)|\sigma|}$ (for $\tau=0,\sigma<0$), and $e^{(-4\gamma_{eg}/f_\tau)|\tau|}$ (for $\sigma=0,\tau>0$, and $\sigma=\tau,\sigma,\tau<0$). Here f_τ and f_σ are dimensionless parameters that differ for each value of u. For the present case where $u=0$, we have $f_\sigma=1.00$ and $f_\tau=1.54$.

Along the other three (partial) axes, $(\tau=0,\sigma>0)$; $(\sigma=0,\tau<0)$; and $(\sigma=\tau,\tau>0)$, the signal decays more rapidly as the Gaussian distribution width is increased from 0. The signal vanishes completely as $\Omega/\gamma_{eg}\rightarrow\infty$. Such behavior may be easily explained in the context of FTC diagram analysis. Thus as stated in Sec. III, the PE diagrams only contribute to the domains where $\sigma<0$ and $(\sigma-\tau)<0$, while the FID terms contribute to the entire τ-σ plane. As one increases the distribution of the electronic Bohr frequency, the FID terms decay more rapidly (since FID cannot rephase the inhomogeneous contributions to the signal), until $\Omega/\gamma_{eg}\rightarrow\infty$, at which point these terms instantaneously decay to zero (they vanish). In contrast, the PE terms possesses rephasing capabilities, and as such do not vanish in the limit of extreme heterogeneity.

In principle, this distinguishing behavior of the FID and PE terms permits one to extract all three material parameters γ_{ee}, γ_{eg}, and Ω, from an experiment. The decays along the negative σ axis and the τ axis for $(\tau-\sigma)>0$ each have rate

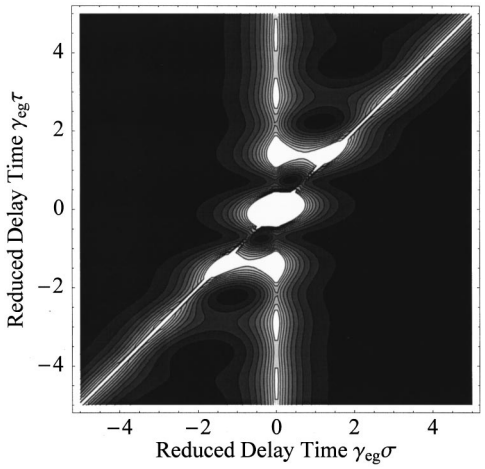

FIG. 4. The simulated homodyne third order signal generated from a model liquid for which $u=0$. The homogeneous limit applies ($\Omega=0$). The wave number of detection is set such that $\tilde{\Delta}=22.5\,\mathrm{cm}^{-1}$. Interferometric beating between the RDOs along σ and τ (each at a wave number of 22.5 cm^{-1}) manifests itself in this 2D signal.

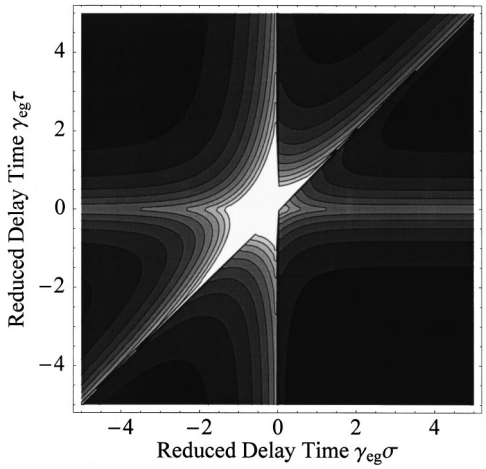

FIG. 5. The simulated homodyne signal at zero RDO ($\tilde{\Delta}=0\,\mathrm{cm}^{-1}$) generated from a model liquid having $u=0.5$. The homogeneous limit applies ($\Omega=0$). The decay is not as rapid as those previously presented, thus filling more of the τ-σ plane with signal.

constants which depend differently on γ_{ee} and γ_{eg}. The 2D regions defined by these axes contain information on the purely dynamical parameters γ_{ee} and γ_{eg}, even in the limit of extreme inhomogeneity. The terms contributing to the remaining 2D region (defined by $\sigma>0$ and $\tau-\sigma<0$), do not posses rephasing capabilities and therefore decay with the rate constant that is proportional to Ω (for $\Omega>\gamma_{eg}$). Fitting the experiment to the full (2D) theory will thus allow one to extract both the dynamical rate constants and the width of the static distribution function.

The $u=0$, $\Delta\neq0$ *case*. The phenomenon of electronic Bohr frequency downconversion is demonstrated in Fig. 4. Shown here is the third order signal detected at $\tilde{\nu}_D\equiv\omega_D/2\pi c=14\,022.5\,\mathrm{cm}^{-1}$ with the system in the homogeneous limit ($\Omega=0$). Radiation difference oscillations (RDOs) at $\tilde{\Delta}\equiv\Delta/2\pi c=22.5\,\mathrm{cm}^{-1}$ ($\Delta=4.2426\,\mathrm{ps}^{-1}$) are seen along both the τ and σ axes. The decays are identical to the previous case where the RDOs are absent ($\Delta=0$). A complete array of such RDO fringes, obtained by varying ω_D, allows one to precisely measure the mean electronic transition frequency ω_{eg}^0 in a given experiment. Presumably, the RDO picture will change in an interesting way when a more realistic multistate model (a two manifold model for example) is considered.

In the other extreme, in which large heterogeneity is present and dominates the pure dephasing rate constant ($\Omega/\gamma_{eg}\rightarrow\infty$), RDOs are completely absent, since (as it turns out for the limit of large inhomogeneity), the only surviving terms, the PE terms, are independent of the detected frequency. In this inhomogeneous limit, only these quadrature PE terms are present so the signal remains completely nonoscillatory, regardless of the frequency of detection ω_D.

The $u=0.5$, $\Delta=0$ *case*. Presented in Fig. 5 is the homodyne detected signal at the zero difference frequency ($\Delta=0$) in the homogeneous limit ($\Omega=0$) for $u=0.5$ ($\gamma_{ee}=0.5\gamma_{eg}$). A new decay is seen that is centered about $\tau=0$. This is a consequence of noise correlations that are allowed to accumulate only along the τ dimension. As previously mentioned, these correlations (or FTC diagrams) are predicted to be quite weak contributors to the signal (based on FTC analysis). However once $u>0$, their contribution grows considerably since their overall strength is found to increase with the magnitude of u.

Singular exponential behavior is not maintained once u is nonzero, even in the homogeneous limit ($\Omega=0$). Qualitatively speaking, the (effective) decay rate constants along all three principle time axes, τ with $\sigma=0$, σ with $\tau=0$ and τ with $\tau=\sigma$, decreases slightly as u becomes larger until $u\approx0.5$, at which point the decay rate constants increase again. As observed from Figs. 3 and 5, one may notice that the decay rate slightly decreases as u is changed from 0 (Fig. 3) to 0.5 (Fig. 5). However a slight increase in the rate of decay is found as u increases further from 0.5 to $u=1$ (not shown).

This subtle behavior is absent in the inhomogeneous limit, where one sees a steady decrease in the (effective) decay rate as u is increased. With the decay law approximated as an exponential for $u=0.5$, the f factors become $f_\sigma=1.42$, $f_\tau=2.10$. For $u=1$ (not shown), we have $f_\sigma=2.00$, $f_\tau=2.96$. Aside from the nature of their decay, the signals at $u=1$ (not shown) resemble those presented for the homogeneous limit. (A more indepth discussion of the rate of decay as a function of u may be found in Ref. [25] for the 1D analog of these FWM experiments. It is interesting to note however, that the qualitative aspects of this decay rate behavior are maintained as the technique is extended into a second time dimension.)

Once again, these simulations demonstrate how one may extract both dynamical and static information from the 2D FWM signal, through such detailed analysis of the decay in both the homogeneous and inhomogeneous limits. In the intermediate regime, these parameters are also available once the observed 2D signals in τ-σ space are fit to the full theory.

The $u=0.5$, $\Delta\neq0$ *case*. Finally, we present the homodyned signal from this model system at $u=0.5$ and for the RDO at $\tilde{\Delta}=22.5\,\mathrm{cm}^{-1}$. Both the homogeneous and inhomogeneous limits are examined, the former in Fig. 6, the latter

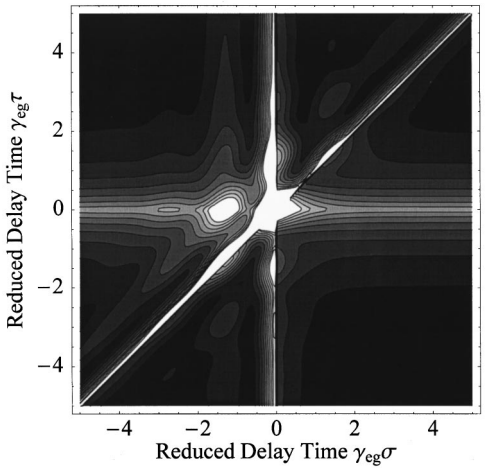

FIG. 6. A contour plot representing the signal generated from the same model liquid as that examined in Fig. 5, but now the detected wave number is such that $\tilde{\Delta}=22.5\,\mathrm{cm}^{-1}$. A complex beat pattern results from the interference of the RDOs along the τ, σ, and $(\tau-\sigma)$ axes. The decay is identical to that seen at $\tilde{\Delta}=0\,\mathrm{cm}^{-1}$ (Fig. 5).

in Fig. 7. Readily seen in Fig. 6 is a complex beat pattern, resulting from RDO frequencies along the reduced τ, σ, and $\tau-\sigma$ axes. As in the completely down-converted case $\tilde{\Delta}=0\,\mathrm{cm}^{-1}$ (Fig. 5), nonexponential decay along both time dimensions manifests itself, due to the nonzero value of u. One also can notice that the signal (excluding the τ-only decay terms) in the domain defined by $\sigma>0$ and $\sigma-\tau>0$ is much weaker in the $u=0.5$ case than for $u=0$. This follows because the quadrature FID terms become relatively weaker compared to the quadrature PE terms as u is increased. (As such, the τ-only decay terms become increasing significant.)

Displayed in Fig. 7 is the homodyned signal for the same model but now in the inhomogeneous limit. The 2D signal

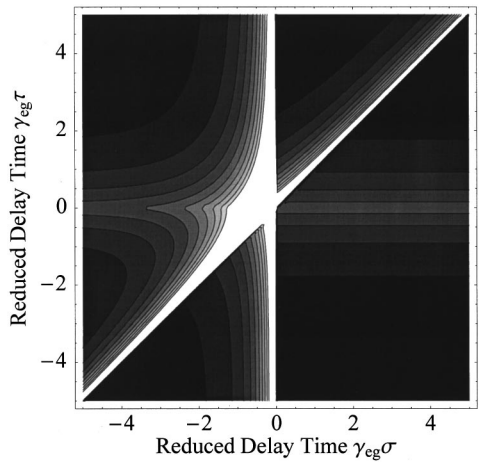

FIG. 7. The homodyne signal from a model liquid for which $u=0.5$, $\tilde{\Delta}=22.5\,\mathrm{cm}^{-1}$. The inhomogeneous limit $(\Omega/\gamma_{eg}\gg 1)$ applies. Only quadrature PE channels survive at nonzero delay times. Since these do not carry RDOs in this limit, no oscillations are seen. The decay of the signal is slightly modified from that seen in the homogeneous case (Fig. 4).

generated from this inhomogeneously broadened case is quite similar (only differing slightly in its decay) to that shown in Fig. 5 for the homogenous limit detected at $\tilde{\Delta}=0\,\mathrm{cm}^{-1}$. In both situations, the signal is free of oscillations; the former since only quadrature PE terms survive (carrying no RDO frequencies for large inhomogeneity), while the latter is the signal detected at the zero difference frequency. One may also notice that the only terms appearing in the domain defined by $\sigma>0$ and $(\sigma-\tau)>0$ in Fig. 7 are the τ-decaying quadrature PE terms since all others (quadrature FID and FID-PE) are identically zero, as per Sec. III.

V. HETERODYNE DETECTION

Next, we examine the alternative method of detection in which a local oscillator field $E_{lo}(s)$, is introduced in a manner that allows it to go into quadrature with the signal field that is generated from the material polarization $P^{(3)}(t,\tau,\sigma)$. This manner of detection improves sensitivity (the signal is linear rather than quadratic in $P^{(3)}$) and also eliminates all cross terms that complicate the homodyne signal.

The heterodyne signal is not built on a ''bichromophoric'' picture. The s timeline is now reserved for the local oscillator field—not a second chromophore. This field is also under delay-line control, delayed from B by an amount ξ. Thus we write

$$E_{lo}(s,\xi)\propto p(s-\xi)e^{-i\bar{\omega}(s-\xi)}. \tag{18}$$

The heterodyne detected signal intensity is then

$$I^{(3)}_{\mathrm{het}}(\omega_D,\tau,\sigma,\xi)\propto \mathrm{Re}\left[\int_{-\infty}^{\infty} d(t-s)e^{i\omega(t-s)} \times\langle P^{(3)}(t,\tau,\sigma)E^{*}_{lo}(s,\xi)\rangle\right]. \tag{19}$$

Using Eqs. (4), (9), and (18), (19), one has

$$I^{(3)}_{\mathrm{het}}(\omega_D,\tau,\sigma,\xi)\propto N\,\mathrm{Re}\left[\int_{-\infty}^{\infty} d(t-s)e^{i\omega_D(t-s)}e^{i\varpi(s-\xi)} \times\int_0^{\infty} d\omega^t_{eg}g(\omega^t_{eg}) \tag{20a}$$

$$\times(\langle p^{*}(s-\xi)D_1\rangle+\langle p^{*}(s-\xi)D_2\rangle \tag{20b}$$

$$+\langle p^{*}(s-\xi)D_3\rangle+\langle p^{*}(s-\xi)D_4\rangle)]. \tag{20c}$$

Though yielding a much less complicated expression for the signal (as seen by Table II), this heterodyne signal does not possess the advantages of downconversion (as discussed above) for interferometric sampling. The signal contains oscillations at the optical frequency of the electronic transition, thus making the Nyquist criterion for interferometry a much more severe one than for the homodyne experiment.

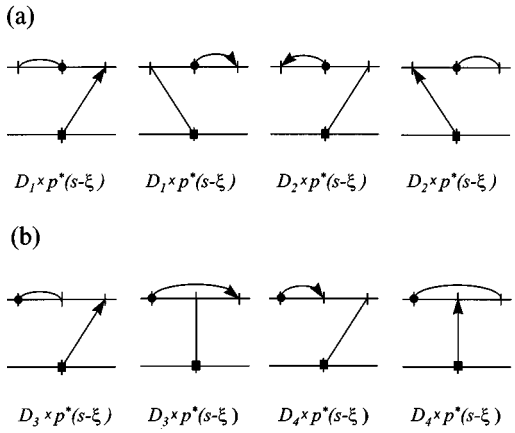

FIG. 8. The FTC diagrams for the heterodyne detected FWM process. The *square* head represents the time (s_1) at which the ξ shifted local oscillator field acts. Each diagram is labeled by the product of a given WMEL diagram that it represents and the random noise function associated with the local oscillator. (a) The two FID channels; (b) the two PE channels.

A. Free induction decay

The heterodyne detected signal for the FID terms in Eq. (20b) reduces to

$$I^{(3)}_{\mathrm{FID,het}}(\omega_D,\tau,\sigma,\xi) \propto N\,\mathrm{Re}\Bigg[\int_{-\infty}^{\infty} d(t-s)e^{i\omega_D(t-s)}e^{i\varpi(s-\xi)} \times \int_0^{\infty} d\omega^t_{eg} g(\omega^t_{eg}) \int d\Omega_t \times \sum_{i=1}^{2} \Gamma^{(2,2)}_i e^{-i\varpi(t_3-t_2+t_1)} \times R^{(3)}_{\mathrm{FID}}(t_1,t_2,t_3,\omega^t_{eg})\Bigg]. \tag{21}$$

where $\Gamma^{(2,2)}_i$ is a four-point time correlation function associated with the noisy fields. Here only four field actions—three from the third order polarization field, one from the local oscillator, are needed to describe the heterodyne detected signal. As such, there are only four four-point time correlators which describe the total FWM process: $\Gamma^{(2,2)}_i (i=1,2)$ for the FID process and $\Gamma^{(2,2)}_i (i=3,4)$ for the PE process (see Table II). As with the six-point correlation functions appearing in the expression for the homodyned signal, the time dependence of these four-point correlators remains implicit in the current calculations. Their form may be found (explicitly) in the Appendix.

Only four FTC diagrams [Fig. 8(a)] are needed to describe all noise correlations for this process, each depending on all three delay times τ, σ, and ξ. For heterodyne detection, it is impossible to draw FTC diagrams which are simply composed of segments having no arrow or solid circle heads. This means that the signal is entirely free of the constant background found in the homodyne case.

One may again notice that the entire τ-σ plane contains contributions from at least one of the four FTC diagrams. It is not necessary to consider the ξ variable for it merely determines the phase of the signal in ξ space—no new material information is gained. For this reason, the local oscillator field is kept stationary (ξ fixed) during the course of analyzing an experiment. Again, the noise correlations for this process allow for full accumulation over the t and s timelines regardless of the (absolute) magnitude of the delay times. Such accumulation behavior is not apparent for the PE pathways.

B. Photon echo

The heterodyne detected signal for the PE pathways [term (20c)] is given by

$$I^{(3)}_{\mathrm{PE,het}}(\omega_D,\tau,\sigma,\xi) \propto N\,\mathrm{Re}\Bigg[\int_{-\infty}^{\infty} d(t-s)e^{i\omega_D(t-s)}e^{i\varpi(s-\xi)} \times \int_0^{\infty} d\omega^t_{eg} g(\omega^t_{eg}) \int d\Omega_t \times \sum_{i=3}^{4} \Gamma^{(2,2)}_i e^{-i\varpi(t_3+t_2-t_1)} \times R^{(3)}_{\mathrm{PE}}(t_1,t_2,t_3,\omega^t_{eg})\Bigg]. \tag{22}$$

As with the FID pathways, only four FTC diagrams [Fig. 8(b)] characterize the noise correlations for the PE process. Once again, the constant background present in homodyne detection is absent for the heterodyne detected case, since all four diagrams only contain delay time dependent noise correlators. (The pair correlator segments always are ''headed'' one way or another. See Fig. 8) One may also notice that these noise correlations are restricted to the delay time domains where $\sigma<0$ and $(\tau-\sigma)<0$, as per the homodyne detected signal.

Electronic Bohr frequency downconversion to the RDOs is absent and oscillations only in the optical region along the $(\tau-\sigma)$ axis (ω^0_{eg} and ω_D), τ axis (ω_D), σ axis (ω^0_{eg}), and ξ axis (ω_D) are all readily seen. Though one may set ξ to zero without loss of information, the two-dimensional signal continues to contain oscillations at optical frequencies. Adequate interferometric sampling is now experimentally difficult since the temporal step size must be of subfemtosecond resolution and be achieved with high precision.

The rate of decay of the heterodyne signal is qualitatively similar to that of the homodyne detected signal for all degrees of heterogeneity. However, now the decay rate constants are exactly half that seen for detection in self-quadrature (The heterodyned signal is proportional to $R^{(3)}$ not $|R^{(3)}|^2$.) But now, unlike the homodyned signal, the constant background is absent. This suggests that heterodyne detection, while unable to down-convert the electronic Bohr frequency, has a great advantage in its dynamic range.

VI. CONCLUDING REMARKS

The theory for electronically resonant, multidimensional FWM spectroscopy for a standard two-level system having a dephasing rate constant, an excited state lifetime and a Gaussian distribution of electronic Bohr frequencies has been developed for broadband (''noisy'') light interferometry. In this theoretical formalism, we have accounted for the simultaneous presence of the photon echo process, which is capable of rephasing the macroscopic coherence loss due to heterogeneity, the free induction decay process, which lacks rephasing capabilities, and (in homodyne detection) their cross terms. Such scattering pathways are inseparable in time for this ''continuous wave'' technique, unlike their separability in the conventional ultrashort pulse experiments.

For homodyne detection, strongly downconverted representations of the electronic frequency reveal themselves in the signal. Referred to as radiation difference oscillations (RDO's), these light-matter beats offer a great advantage in performing the interferometry since the Nyquist criterion is satisfied for much smaller sampling rates. These RDOs also provide a direct and highly precise measure of the (mean) electronic transition frequency.

Both the dephasing rate constant γ_{eg} and the inverse lifetime constant γ_{ee} as well as the Gaussian spread of the electronic Bohr frequencies over the ensemble are measurable from the 2D FWM signal. In the limit, $\gamma_{eg} \gg \gamma_{ee}$ $(u=0)$, pure exponential behavior is seen throughout the (reduced) τ-σ plane for homogeneous broadening ($\Omega=0$). Exponential behavior is maintained even in the limit of large inhomogeneity ($\Omega/\gamma_{eg} \to \infty$); however, now the signal is identically zero in the region where both $\sigma>0$ and $(\sigma-\tau)>0$. For this limit, the quadrature FID and FID-PE cross terms have instantaneously collapsed to zero while the quadrature PE terms only contribute to the regions where either $\sigma<0$ or $(\tau-\sigma)>0$. As $u=\gamma_{ee}/\gamma_{eg}$ is increased from zero, singular exponential behavior is no longer sustained, while the qualitative behavior of the decay of the signal remains similar to that in the $u=0$ case.

From one point of view, heterodyning is a less desirable method of detection since RDOs are absent and the signal oscillates only at optical frequencies making interferometry a challenge. On the other hand, unlike the homodyned signal, the heterodyne experiment is free of a ''permanent'' background and offers a dynamic range that is comparable to that in femtosecond experiments (heterodyne or homodyne).

Both methods provide a new way to experimentally obtain the coherence and population decay rate constants and the spread of the inhomogeneous distribution of electronic Bohr frequencies. Extension of the theory to a more realistic two-vibronic manifold model should be revealing. Of course experimental efforts in this new 2D interferometric spectroscopy are needed.

ACKNOWLEDGMENT

The authors are grateful to the National Science Foundation for support of this work (Grant No. CHE-9616635).

APPENDIX

In this Appendix, all six- and four-point time correlation functions are presented as they appear in homodyne and heterodyne detection, respectively, for the third order FWM signal. These correlation functions are general in that their analytic form need not be specified.

Homodyne detection. We have seen how sixteen six-point time correlation functions arise from all possible field permutations of the conjugate pairings (due to quadrature detection) of the two fully resonant (PE and FID) Liouville pathways. Of these, eight appear in the FID-PE cross terms and they do so as conjugate pairs. Thus four of these need not be explicitly considered. Of the remaining twelve, the first four $\Gamma_1^{(3,3)}-\Gamma_4^{(3,3)}$ arise from quadrature FID type correlations; $\Gamma_5^{(3,3)}-\Gamma_8^{(3,3)}$ from quadrature PE type correlations; and $\Gamma_9^{(3,3)}-\Gamma_{12}^{(3,3)}$, their cross terms:

$$\Gamma_1^{(3,3)}=\langle p(t_1)p^*(t_2-\sigma)p(t_3-\tau)p^*(s_1)p(s_2-\sigma)p^*(s_3-\tau)\rangle,$$

$$\Gamma_2^{(3,3,)}=\langle p(t_1-\tau)p^*(t_2-\sigma)p(t_3)p^*(s_1-\tau)p(s_2-\sigma)p^*(s_3)\rangle,$$

$$\Gamma_3^{(3,3)}=\langle p(t_1)p^*(t_2-\sigma)p(t_3-\tau)p^*(s_1-\tau)p(s_2-\sigma)p^*(s_3)\rangle,$$

$$\Gamma_4^{(3,3)}=\langle p(t_1-\tau)p^*(t_2-\sigma)p(t_3)p^*(s_1)p(s_2-\sigma)p^*(s_3-\tau)\rangle,$$

$$\Gamma_5^{(3,3)}=\langle p^*(t_1-\sigma)p^*(t_2)p(t_3-\tau)p(s_1-\sigma)p^*(s_2)p^*(s_3-\tau)\rangle,$$

$$\Gamma_6^{(3,3)}=\langle p^*(t_1-\sigma)p^*(t_2-\tau)p(t_3)p(s_1-\sigma)p^*(s_2-\tau)p^*(s_3)\rangle,$$

$$\Gamma_7^{(3,3)}=\langle p^*(t_1-\sigma)p^*(t_2)p(t_3-\tau)p(s_1-\sigma)g^*(s_2-\tau)p^*(s_3)\rangle,$$

$$\Gamma_8^{(3,3)}=\langle p^*(t_1-\sigma)p^*(t_2-\tau)p(t_3)p(s_1-\sigma)p^*(s_2)p^*(s_3-\tau)\rangle,$$

$$\Gamma_9^{(3,3)}=\langle p(t_1)p^*(t_2-\sigma)p(t_3-\tau)p(s_1-\sigma)p^*(s_2)p^*(s_3-\tau)\rangle,$$

$$\Gamma_{10}^{(3,3)}=\langle p(t_1)p^*(t_2-\sigma)p(t_3-\tau)p(s_1-\sigma)p^*(s_2-\tau)p^*(s_3)\rangle,$$

$$\Gamma_{11}^{(3,3)}=\langle p(t_1-\tau)p^*(t_2-\sigma)p(t_3)p(s_1-\sigma)p^*(s_2)p^*(s_3-\tau)\rangle,$$

$$\Gamma_{12}^{(3,3)}=\langle p(t_1-\tau)p^*(t_2-\sigma)p(t_3)p(s_1-\sigma)p^*(s_2-\tau)p^*(s_3)\rangle. \tag{A1}$$

Application of the complex Gaussian moment theorem (CGMT) [54,55] permits each one of these six-point correlation functions to be decomposed into the sum of six terms, each consisting of the product of three two-point correlators, $\Gamma^{(1,1)}$. This decomposition is illustrated for the above six-point time correlator, $\Gamma_1^{(3,3)}$, where now the time arguments are explicitly exposed:

$$\begin{aligned}\Gamma_1^{(3,3)}&(t_1,t_2,t_3;s_1,s_2,s_3;\tau,\sigma)\\ &=\Gamma^{(1,1)}(t_1-t_2+\sigma)\Gamma^{(1,1)}(s_2-s_1-\sigma)\Gamma^{(1,1)}(t_3-s_3)\\ &\quad+\Gamma^{(1,1)}(t_3-t_2+\sigma-\tau)\Gamma^{(1,1)}(s_2-s_3+\tau-\sigma)\Gamma^{(1,1)}(t_1\\ &\quad-s_1)+\Gamma^{(1,1)}(t_1-t_2+\sigma)\Gamma^{(1,1)}(s_2-s_3+\tau-\sigma)\Gamma^{(1,1)}\\ &\quad\times(t_3-s_1-\tau)+\Gamma^{(1,1)}(s_2-s_1-\sigma)\Gamma^{(1,1)}(t_2-t_3+\tau\\ &\quad-\sigma)\Gamma^{(1,1)}(t_1-s_3+\tau)+\Gamma^{(1,1)}(t_2-s_2)\Gamma^{(1,1)}(t_1-s_3\\ &\quad+\tau)\Gamma^{(1,1)}(t_3-s_1-\tau)+\Gamma^{(1,1)}(t_1-s_1)\Gamma^{(1,1)}(t_2\\ &\quad-s_2)\Gamma^{(1,1)}(t_3-s_3).\end{aligned} \tag{A2}$$

Here we have assumed that the noisy fields are stationary processes of time

$$\begin{aligned}\Gamma^{(1,1)}(t_1-t_2)&=\langle p(t_1-t_2)p^*(0)\rangle=\langle p(t_1)p^*(t_2)\rangle\\ &=\lim_{T\to\infty}\frac{1}{T}\int_{-T/2}^{-T/2}p(t-t_2)p^*(t-t_1)dt.\end{aligned} \tag{A3}$$

Each term in Eq. (A2) may be conveniently expressed as a single FTC diagram [the first term in Eq. (A2) is represent by the first FTC diagram of Fig. 2(a)], as per Sec. III and Table I.

Heterodyne detection. Analytically much simpler, the four-point time correlation functions for heterodyne detection represent either the pure FID Liouville pathway ($\Gamma_1^{(2,2)}$ and $\Gamma_2^{(2,2)}$) or the pure PE Liouville pathway ($\Gamma_3^{(2,2)}$ and $\Gamma_4^{(2,2)}$)—no cross terms arise. We have

$$\Gamma_1^{(2,2)}=\langle p(t_1)p^*(t_2-\sigma)p(t_3-\tau)p^*(s-\xi)\rangle,$$

$$\Gamma_2^{(2,2)}=\langle p(t_1-\tau)p^*(t_2-\sigma)p(t_3)p^*(s-\xi)\rangle,$$

$$\Gamma_3^{(2,2)}=\langle p^*(t_1-\sigma)p(t_2)p(t_3-\tau)p^*(s-\xi)\rangle,$$

$$\Gamma_4^{(2,2)}=\langle p^*(t_1-\sigma)p(t_2-\tau)p(t_3)(s-\xi)\rangle. \tag{A4}$$

Similarly, these four-point correlation functions may be decomposed into the sum of two terms, each being the product of two-point time correlators by implementation of the CGMT (see Table I).

In Sec. IV, all two-point time correlators $\Gamma_i^{(1,1)}$ are represented (analytically) by δ functions in time. This assumes that the correlation time of our light τ_c is zero. Although not experimentally realistic, the treatment is not compromised since the essential physics of the multidimensional spectroscopy is maintained. However, whenever the autocorrelation time of the light approaches, from the ultrafast, those found in the material response function, the explicit functional form of $\Gamma^{(1,1)}$ must become a significant factor in analyzing the data.

[1] N. A. Kurnit, I. D. Abella, and S. R. Hartmann, Phys. Rev. Lett. **13**, 567 (1964).

[2] C. A. Walsh, M. Berg, L. R. Narasimham, K. A. Littau, and M. D. Fayer, Acc. Chem. Res. **20**, 120 (1987).

[3] D. A. Wiersma, Adv. Chem. Phys. **47**, 421 (1981).

[4] P. Ye and Y. R. Shen, Phys. Rev. A **25**, 2183 (1982).

[5] M. Berg, C. Walsh, L. R. Narasimham, K. A. Littau, and M. D. Fayer, J. Chem. Phys. **88**, 1564 (1988); Y. S. Bai and M. D. Fayer, Chem. Phys. Lett. **128**, 135 (1988).

[6] N. E. Shemetulskis and R. F. Loring, J. Chem. Phys. **97**, 1217 (1992).

[7] J. T. Fourkas, H. Kawashima, and K. A. Nelson, J. Chem. Phys. **103**, 4393 (1995).

[8] J. C. Kirkwood, D. J. Ulness, and A. C. Albrecht, in *The Encyclopedia of Chemical Physics and Physical Chemistry*, edited by J. H. Moore and N. D. Spencer (IOP Publishing, Phildelphia, in press).

[9] Y. Zhou, L. Ujj, J. Lou, F. Jager, K. Nakanishi, and G. Atkinson, J. Mol. Struct. **478**, 107 (1999).

[10] X. Zhao and T. Spiro, J. Raman Spectrosc. **29**, 49 (1998).

[11] S. Asher, Z. Chi, and P. Li, J. Raman Spectrosc. **29**, 927 (1998).

[12] A. Laubereau and H. Purucker, Nuovo Cimento D **14**, 979 (1992).

[13] S. Nakashima, T. Kitagawa, and J. Olsen, Chem. Phys. **228**, 323 (1998).

[14] C. Reczek, A. Sitter, and J. Terner, J. Mol. Struct. **214**, 27 (1989).

[15] D. Bersani, P. Lottici, and A. Montenero, J. Raman Spectrosc. **30**, 355 (1999).

[16] Y. Tanimura and S. Mukamel, J. Chem. Phys. **99**, 9496 (1993).
[17] S. Mukamel, *Principles of Nonlinear Optical Spectroscopy* (Oxford University Press, New York, 1995).
[18] J. C. Kirkwood, D. J. Ulness, M. J. Stimson, and A. C. Albrecht, Chem. Phys. Lett. **293**, 417 (1998).
[19] J. Kirkwood, D. Ulness, M. Stimson, and A. C. Albrecht, J. Chem. Phys. **111**, 272 (1999).
[20] J. Kirkwood, D. Ulness, and A. C. Albrecht, J. Chem. Phys. **111**, 253 (1999).
[21] J. C. Kirkwood and A. C. Albrecht, J. Raman Spectrosc. (to be published).
[22] J. E. Ivanecky III and J. C. Wright, Chem. Phys. Lett. **206**, 437 (1993).
[23] T. Steffen and K. Duppen, Chem. Phys. Lett. **273**, 47 (1997).
[24] D. J. Ulness, J. C. Kirkwood, and A. C. Albrecht, J. Chem. Phys. **108**, 3897 (1998).
[25] N. Morita and T. Yajima, Phys. Rev. A **30**, 2525 (1984).
[26] G. S. Agarwal, Phys. Rev. A **37**, 4741 (1988).
[27] R. Beach and S. R. Hartmann, Phys. Rev. Lett. **53**, 663 (1984).
[28] N. Nakatsuka, M. Tomita, M. Fujiwara, and S. Asaka, Phys. Rev. A **29**, 2286 (1984).
[29] S. V. Rao, L. Giribabu, B. G. Maiya, and D. N. Rao, Curr. Sci. **72**, 957 (1997).
[30] D. N. Rao, S. V. Rao, F. J. Aranda, D. V. G. L. N. Rao, M. Nakashima, and J. A. Akkara, J. Opt. Soc. Am. B **14**, 2710 (1997).
[31] D. N. Rao and S. V. Rao, Chem. Phys. Lett. **283**, 227 (1998).
[32] M. A. Dugan and A. C. Albrecht, Phys. Rev. A **43**, 3877 (1991).
[33] M. A. Dugan and A. C. Albrecht, Phys. Rev. A **43**, 3922 (1991).
[34] M. A. Dugan, J. S. Melinger, and A. C. Albrecht, Chem. Phys. Lett. **147**, 411 (1988).
[35] S. A. Schaertel and A. C. Albrecht, J. Raman Spectrosc. **25**, 545 (1994).
[36] S. A. Schaertel, A. C. Albrecht, A. Lau, and A. Kummrow, Appl. Phys. B: Photophys. Laser Chem. **59**, 377 (1994).
[37] D. J. Ulness, J. C. Kirkwood, M. J. Stimson, and A. C. Albrecht, J. Chem. Phys. **107**, 7127 (1997).
[38] J. C. Kirkwood, D. J. Ulness, and A. C. Albrecht, J. Chem. Phys. **108**, 9425 (1998).
[39] J. C. Kirkwood, D. J. Ulness, M. J. Stimson, and A. C. Albrecht, Phys. Rev. A **57**, 1417 (1997).
[40] M. J. Stimson, D. J. Ulness, and A. C. Albrecht, Chem. Phys. Lett. **263**, 185 (1996).
[41] D. J. Ulness, M. J. Stimson, J. C. Kirkwood, and A. C. Albrecht, J. Phys. Chem. **101**, 4587 (1997).
[42] D. J. Ulness, J. C. Kirkwood, M. J. Stimson, and A. C. Albrecht, Asian J. Phys. **7**, 405 (1998).
[43] D. J. Ulness, M. J. Stimson, J. C. Kirkwood, and A. C. Albrecht, J. Raman Spectrosc. **28**, 917 (1997).
[44] M. J. Stimson, D. J. Ulness, and A. C. Albrecht, Chem. Phys. **222**, 17 (1997).
[45] M. Pfeiffer and A. Lau, J. Chem. Phys. **108**, 4159 (1998); A. Lau, M. Pfeiffer, and A. Kummrow, Chem. Phys. Lett. **263**, 435 (1996).
[46] A. Lau, M. Pfeiffer, V. Kozich, and F. Tschirschwitz, J. Chem. Phys. **108**, 4173 (1998).
[47] D. C. DeMott, D. J. Ulness, and A. C. Albrecht, Phys. Rev. A **55**, 761 (1997).
[48] D. J. Ulness and A. C. Albrecht, J. Raman Spectrosc. **28**, 571 (1997).
[49] M. J. Stimson, D. J. Ulness, and A. C. Albrecht, J. Raman Spectrosc. **28**, 579 (1997).
[50] D. K. L. Tan, Ph.D. thesis, Cornell University, 1994.
[51] A. Schenzle and R. G. Brewer, Phys. Rep. **43**, 455 (1978).
[52] J. L. Skinner, H. A. Anderson, and M. D. Fayer, J. Chem. Phys. **75**, 3195 (1981).
[53] E. Parker, Ph.D. thesis, Cornell University, 1996.
[54] L. Mandel and E. Wolf, *Optical Coherence and Quantum Optics* (Cambridge University Press, New York, 1995).
[55] C. L. Mehta, in *Lectures in Theoretical Physics*, edited by W. E. Brittin (The University of Colorado Press, Boulder, CO, 1965), Vol. 93, p. 345.
[56] D. Lee and A. C. Albrecht, in *Advances in Infrared and Raman Spectroscopy*, edited by R. J. Clark and R. E. Hester (Wiley, New York, 1984), Vol. 12, p. 129.
[57] J. C. Kirkwood, D. J. Ulness, and A. C. Albrecht, J. Phys. Chem. A (to be published).
[58] E. Hanumura and S. Mukamel, Phys. Rev. A **33**, 1099 (1986).
[59] D. J. Ulness and A. C. Albrecht, Phys. Rev. A **53**, 1081 (1996).
[60] D. J. Ulness, Ph.D. thesis, Cornell University, 1996.
[61] J. C. Kirkwood, D. J. Ulness, M. J. Stimson, and A. C. Albrecht, Phys. Rev. A **58**, 4910 (1998).
[62] J. C. Kirkwood and A. C. Albrecht, Phys. Rev. A (to be published).